Article

Simulation Study of the Transport Characteristics of the Ice Core in Ice Drilling with Air Reverse Circulation

Mengke Wang [1], Wenbo He [1], Jine Cao [1], Bo Qi [2], Jingchao Chen [1] and Pinlu Cao [1,*]

1   Polar Research Center, Jilin University, No. 938 Ximinzhu Str., Changchun 130061, China
2   Changchun Institute of Technology, No. 395 Kuanping Rd., Changchun 130012, China
*   Correspondence: jlucpl@jlu.edu.cn

Abstract: Ice core drilling with air reverse circulation is a promising technology that uses high-speed airflow to transport the ice core from the bottom of the hole along the central passage of the drill pipe to the surface. Understanding how the ice core moves through the pipe is crucial for this technology in order to calculate the pneumatic parameters. In this paper, experimental study and the CFD dynamic mesh technique are used to analyze the ice core transport process and flow field characteristics. In order to prove the correctness of the dynamic mesh technique, the simulation results were verified with the experimental results, and it was found that all the simulation data were in agreement with the experimental data trend, and the maximum error was less than 10%. According to the study, once the ice core's velocity reaches its maximum throughout the transport process, it does not change. The ice core's maximum velocity increases with the diameter ratio and decreases with the length-to-diameter ratio, while eccentricity has no impact on the maximum velocity. When the air velocity reaches 21 m/s, the diameter ratio for the ice core with a length-to-diameter ratio of 2 increases from 0.80 to 0.92, and the maximum velocity increases from 8.92 m/s to 17.45 m/s. Data fitting demonstrates that the equation $V_{max} = -1.04V_0 + 1.04V_a$ describes the relationship between the ice core's maximum velocity, V_{max}, and air velocity, V_a. Finally, we obtain the ice core's suspension velocity model using CFD simulation to calculate the suspension velocity, V_0.

Keywords: air reverse circulation; transport characteristic; maximum velocity; streamline pattern

1. Introduction

The world's climate is currently altering rapidly. People urgently need to comprehend the fundamental principles and driving forces behind historical climate change to increase the precision of future climate change predictions. The polar ice environment contains unique biological, geochemical, and geological information that can be analyzed and dated to understand past climate and explore the causes of climate change. Deeper ice caps, in particular, preserve much older information and have been called natural archives of ancient climate [1,2]. The above information can be gained through sample analysis and observation of the polar ice layer, and polar drilling is the most direct technical method for obtaining ice core samples. However, the highly challenging operating conditions and strict environmental protection standards present severe difficulties for this technology [3,4].

For polar coring drilling, armored cable-suspended electromechanical drills are commonly used, which use an armored cable to transport the drills to the bottom of the hole and transmit power to the motor to drive the drills to rotate [5,6]. Drilled ice cores and cuttings are carried to the ice core barrel and ice cutting chamber by a special low-temperature drilling fluid that circulates locally at the bottom of the hole. After filling the ice core barrel (generally 2~4 m) and ice cutting chamber in the drills, the drills must be lifted to the surface for treatment before reinserting into the borehole for subsequent drilling [7]. The drills' single drilling depth is short, and the drills must be continuously tripped in and out of the borehole, resulting in a low drilling rate of penetration and, finally, efficiency.

Due to the high permeability of the snow-firn layer in the upper part of the ice layer, if drilling is performed with drilling fluid, it will cause huge circulation loss and make drilling extremely difficult. By using air reverse circulation drilling, the presence of a double-wall drill pipe can avoid air leakage and solve the problem of difficult drilling in the snow-firn layer. Therefore, in recent years, ice drilling experts have proposed air reverse circulation continuous coring (sampling) drilling technology with high drilling efficiency and no environmental pollution [8–10]. The schematic diagram of ice air reverse circulation core drilling is shown in Figure 1. During drilling the drilled core (sample) is promptly and continuously delivered to the surface by the airflow from the center channel of the double-wall drill pipes, saving much tripping operating time of lifting and lowering core drilling equipment and improving drilling efficiency. Hydrogeology, engineering geology, and civil engineering drilling have all used this technology extensively. Currently, there is also an international focus on the technology of air drilling into the ice [11,12]. In 2010–2011, U.S. IDP developed a non-core drill, the Rapid Air Movement Drill (RAM), for seismic geophysical exploration, which was subsequently upgraded to the RAM-2 drill to reduce logistical requirements. To solve the problems of air loss, frost accumulation, and ice chip adhesion when drilling permeable glaciers, scientists from St. Petersburg University of Mining and Technology applied the technique of air local reverse circulation at the bottom for the first time for ice drilling and proposed a focus for subsequent research. However, for these air drilling into ice applications, full-face drilling, or non-core drilling, is where it is most frequently utilized, and the drilled ice samples are almost exclusively ice cuttings. Conversely, the coring drilling technique primarily drills large-diameter ice cores.
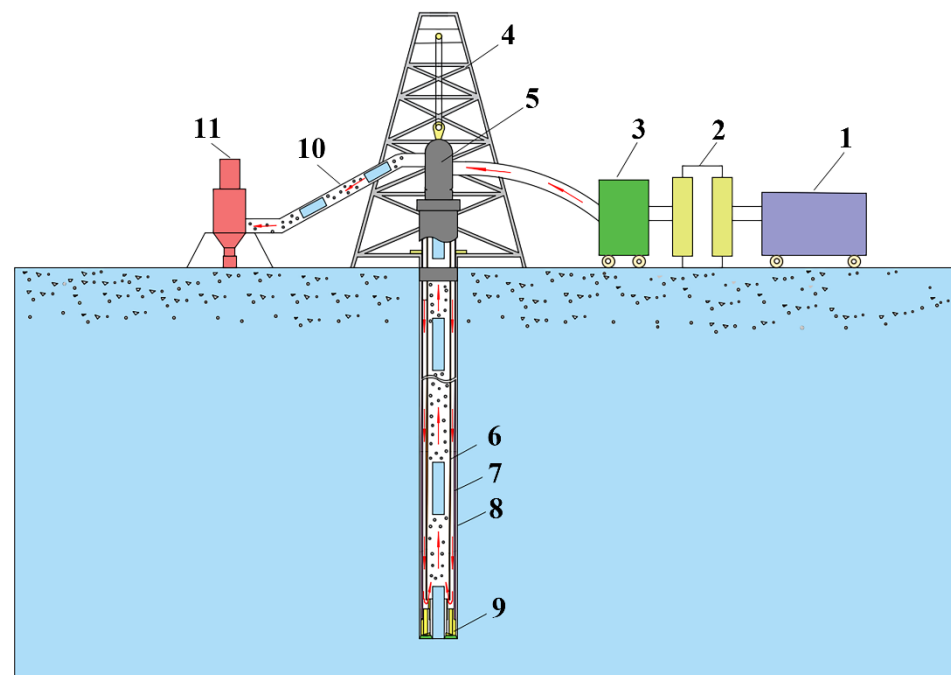
Figure 1. Schematic diagram of air reverse circulation core drilling: (1) air compressor; (2) cooler; (3) dryer; (4) drill tower; (5) swivel with dual wall; (6) inner pipe of drill pipe; (7) outer pipe of drill pipe; (8) borehole wall; (9) drill bit; (10) discharge pipe; (11) cyclone.

The air reverse circulation core drilling studied in this paper is suitable for ice layer drilling, not for snow-firn layer drilling. Therefore, this paper does not consider the situation in the snow-firn layer. The energy used by the airflow and ice core in the gas–solid two-phase flow is offset by the airflow's pressure energy. The pressure loss of the separated gas–solid two-phase flow must be determined in order to move the ice core from the bottom of the hole to the surface safely and effectively [13–15]. Understanding the velocity at which the ice core moves inside the pipe is necessary for calculating the air pressure loss. The

ice core's velocity grows from zero to its maximum velocity under the airflow thrust and stays constant. The ice core's primary mode of motion during long-distance transportation is uniform movement at maximal velocity. The suspension velocity of the ice core is the current focus of research on the pneumatic transportation of ice cores. For instance, using theoretical and practical research, Cao et al. investigated the suspension velocity of ice cores of 60 mm diameter at various drill pipe sizes [13]. They created a mathematical model for the minimum airflow and pressure drop necessary to suspend ice cores at various drilling depths. The researchers also conducted theoretical and experimental evaluations to create a universal model for assessing the suspension velocity of ice cores, allowing them to estimate the velocity of ice core suspension of various sizes [14]. However, all of the above research was carried out in stationary states and has limited applicability in dynamic systems, because comparing the relative velocities and inertial effects of fixed and moving ice cores is difficult.

The transport of an ice core in a pipe can be generalized to the problem of the movement of cylindrical particles with a diameter ratio greater than 0.8 to the pipe diameter in a fluid transport pipe. The settling velocity and drag coefficient of cylindrical particles in a fluid-filled conduit has been thoroughly researched, and valuable conclusions have been drawn. For example, Unnikrishnan experimentally studied the settling velocity of cylindrical particles with diameter ratios of 0.08~0.4 and aspect ratios of 0.05~2 in a pipe filled with Newtonian fluid and compared it with the settling velocity in a pipe without wall restriction [16]. Lau studied the influence of the wall effect on the settling velocity of cylindrical particles in the inertial zone and developed a semi-empirical model that can predict the wall effect in the range of 0 to 1 diameter ratio [17]. However, none of these studies analyzed the transport characteristics of particles under fluid driving. Chow experimentally studied the hydraulic transport characteristics of cylindrical capsules in vertical pipes, a semi-empirical model between the capsule velocity and water flow velocity, and the diameter ratio of capsules to pipes, and the aspect ratios of capsules were obtained [18]. Myška discovered that a linear equation with two coefficients could be used to define the capsule velocity equation seen in most of the literature [19]. However, because water serves as the transport medium in these investigations and water has significantly higher density and viscosity than air, it cannot be used to assess the pneumatic transport properties of the ice core directly.

Currently, high-speed cameras are frequently used by researchers to examine object motion. Only a specific distance may often be captured for examination due to the high-speed camera's pixel and field of vision constraints. The high-speed camera cannot analyze the entire process because of the object's considerable acceleration distance in the pipeline. The fluid–solid coupling flow in the pipe is complicated because it is fundamentally transient and subject to various physical influences [20,21]. Using experimental methods makes it difficult to solve the issue accurately, and the experiment cannot gather any data on the flow field surrounding the object. Numerous academics now employ numerical simulation to study the motion of objects due to its effectiveness in addressing complex flows. The transport process of the ice core under various air velocities will be simulated in this paper and analyzed.

2. Experimental Apparatus

When ice core drilling takes place, there are ice cuttings in addition to ice cores in the drill pipe. Considering the difficulty of simulation, only the case of the ice core alone is considered in this paper. In the actual drilling, the shape of the ice core is not necessarily a regular shaped cylinder; for the sake of simplifying the model, only regular shaped ice cores are considered. Figure 2 illustrates the experimental setup used to confirm the accuracy of the simulation results. The ice core is propelled upward by the airflow from the air compressor when it enters the pipe at a specific speed. The data acquisition system transmits the airflow characteristics to the computer for monitoring by using flow, pressure, and temperature sensors. A high-speed camera captures the ice core's movement, and

professional video processing software is then used to examine it. The experiment uses a polypropylene cylinder with a density of 910 kg/m^3, which is within the range of the polar ice layer's typical density of 900 to 930 kg/m^3. The experimental procedure is as follows:

1. Put the ice core into the bottom of the plexiglass tube and use the ice core holder to center its position and fix it at the bottom of the tube.

2. Turn on the high-speed camera and prepare to record the movement of the ice core.

3. Turn on the air compressor, monitor the airflow parameters by computer, and release the ice core when the airflow is stable.

4. After the high-speed camera records the movement of the ice core, analyze the movement of the ice core through the post-processing software.

5. Repeat the above steps.
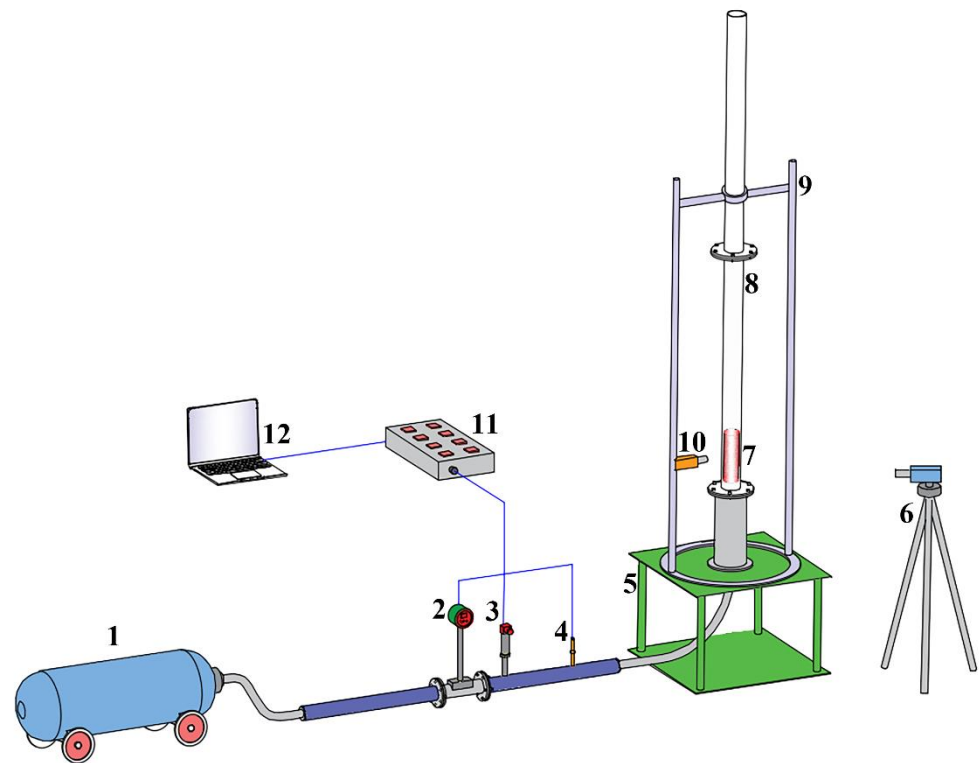
Figure 2. Experimental apparatus. (1) ZV-3/10 air compressor; (2) LK-VFF-50 flow meter, 1.5% FS; (3) MIK-P300 pressure sensor, 0.2% FS; (4) Pt-100 temperature sensor; (5) base frame; (6) YVSION/OSG030-815UMTZ high-speed camera; (7) polypropylene cylinder; (8) plexiglass pipe; (9) support frame; (10) light; (11) data collection box; (12) computer.

3. Numerical Method

3.1. Governing Equations of Fluid Motion and Ice Core Motion

Incompressible flow is governed by the Navier–Stokes (N–S) equations, expressed as follows:

$$\nabla\cdot\boldsymbol{u} = 0 \tag{1}$$

$$\frac{\partial \boldsymbol{u}}{\partial t} + \boldsymbol{u}\cdot\nabla\boldsymbol{u} = -\frac{1}{\rho_f}\nabla p + \nu\nabla^2\boldsymbol{u} + f_g \tag{2}$$

where $\boldsymbol{u}$ is the velocity of the fluid, p represents the pressure, f_g denotes the gravitational force, ρ_f labels the density of the fluid, ν is the kinematic viscosity, and t is the time.

The ice core is assumed to be a rigid body. The six-degree-of-freedom (6DOF) motion solver is employed to simulate the ice core translational motion. The resultant forces acting on the ice core are calculated and are used to solve the governing equations of the motion:

$$m\frac{dV}{dt} = F \tag{3}$$

where m represents the ice core mass, V denotes the velocity of the ice core center, and F is the resultant force on the ice core.

3.2. Physical Model and Boundary Conditions

The length of the pipe model must be sufficient to guarantee that the ice core can reach its maximum velocity. Following testing, the 70 m length satisfies the specifications. The ice-core-to-pipe diameter ratio, ice-core-length-to-diameter ratio, and eccentricity are the parameters that were simulated in this study. The diameter of the ice core is fixed at 70 mm, and the length-to-diameter ratio and diameter ratio are modified by varying the pipe diameter and ice core length. This is to control the weight of the ice core as consistently as possible for analysis. The geometric parameters of the simulated ice cores are shown in Table 1. The RNG k-ε turbulence model is used in the simulation, considering the turbulent vortex above the ice core. To be able to simulate the low temperature environment of the polar regions, the simulation uses the air density and dynamic viscosity at a temperature of $-30°$. The properties of the air in the simulation and the inlet velocity are shown in Table 2.

Table 1. Geometric parameters of the simulated ice cores.

Ice Core Diameter d, mm	Simulated Parameters		
	Diameter Ratio, φ	Length-to-Diameter Ratio, λ	Eccentricity, ε
70	0.80	1	0
	0.84	2	0.3
	0.88	3	0.6
	0.92	4	0.9

Table 2. The properties of the air in the simulation and the inlet velocity.

Temperature °	Air Density kg/m^3	Dynamic Viscosity of Air Pa·s	Air Velocity m/s
-30	1.45	1.57×10^{-5}	15
			18
			21
			24
			27
			30

The ice-core-to-pipe diameter ratio is:

$$\varphi = \frac{d}{D} \tag{4}$$

The ice-core-length-to-diameter ratio is:

$$\lambda = \frac{L}{d} \tag{5}$$

The ice-core-eccentricity is

$$\varepsilon = \frac{2E}{D - d} \tag{6}$$

where d and D are the diameters of the ice core and pipe, L is the length of the ice core, and E is the distance between the ice core's axis and the pipe's axis.

Due to the long pipe length, a two-dimensional axisymmetric model is used when the ice core eccentricity is 0, and a three-dimensional model is used when the ice core is

eccentric, to save calculation time. The total length of the fluid domain is 70 m, and the initial position of the ice core is 2 m away from the inlet to ensure the full development of airflow. The inlet and outlet of the fluid domain adopt velocity inlet and pressure outlet, respectively, and the ice core and pipe walls adopt non-slip walls. The symmetry axis is set as the axis boundary condition. The two-dimensional axisymmetric physical model is shown in Figure 3.
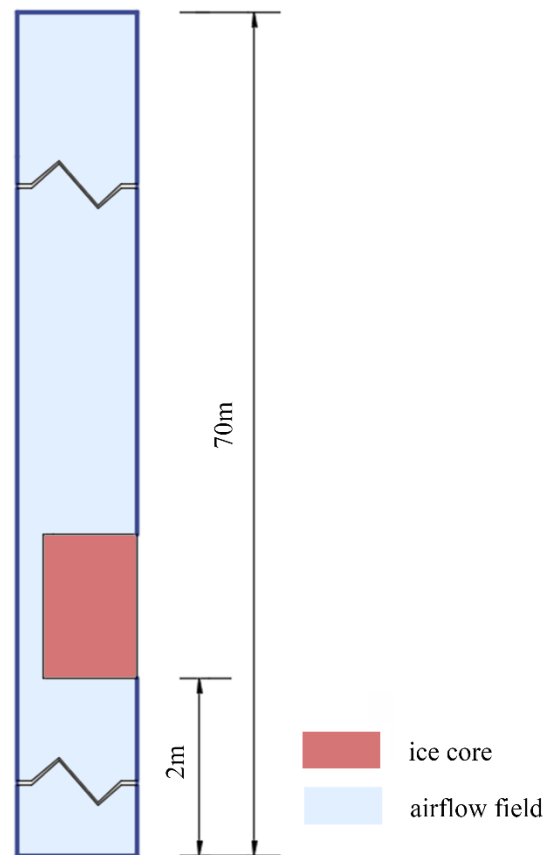
Figure 3. Two-dimensional axisymmetric physical model.

3.3. Computational Mesh

For numerical simulations, the mesh's quantity and quality significantly impact the computation's outcomes. In this simulation, a structured mesh is employed to produce a mesh of excellent quality. The mesh must be encrypted because the gradient of the flow field surrounding the ice core fluctuates substantially. First, a grid sensitivity study was carried out to ensure that calculations were independent of the number of mesh components. Table 3 displays the effect of the mesh element number on the ice core's maximum velocity. Table 3 shows that when the number of mesh elements is raised to 629,010, the ice core' maximum velocity remains almost constant. However, as the number of mesh elements grows, the CPU computation time grows substantially. Therefore, for additional simulation, a mesh with 629,010 elements was used. Figure 4 displays the meshes of the 2D and 3D models utilized in the calculations.

Table 3. The effect of the mesh element number on the ice core's maximum velocity.

No. of Elements	No. of Nodes	Cell Size m	Maximum Velocity m/s
392,985	401,813	0.008	17.16
449,165	459,243	0.007	17.30
524,030	535,774	0.006	17.53
629,010	643,090	0.005	17.59
786,265	803,845	0.004	17.61
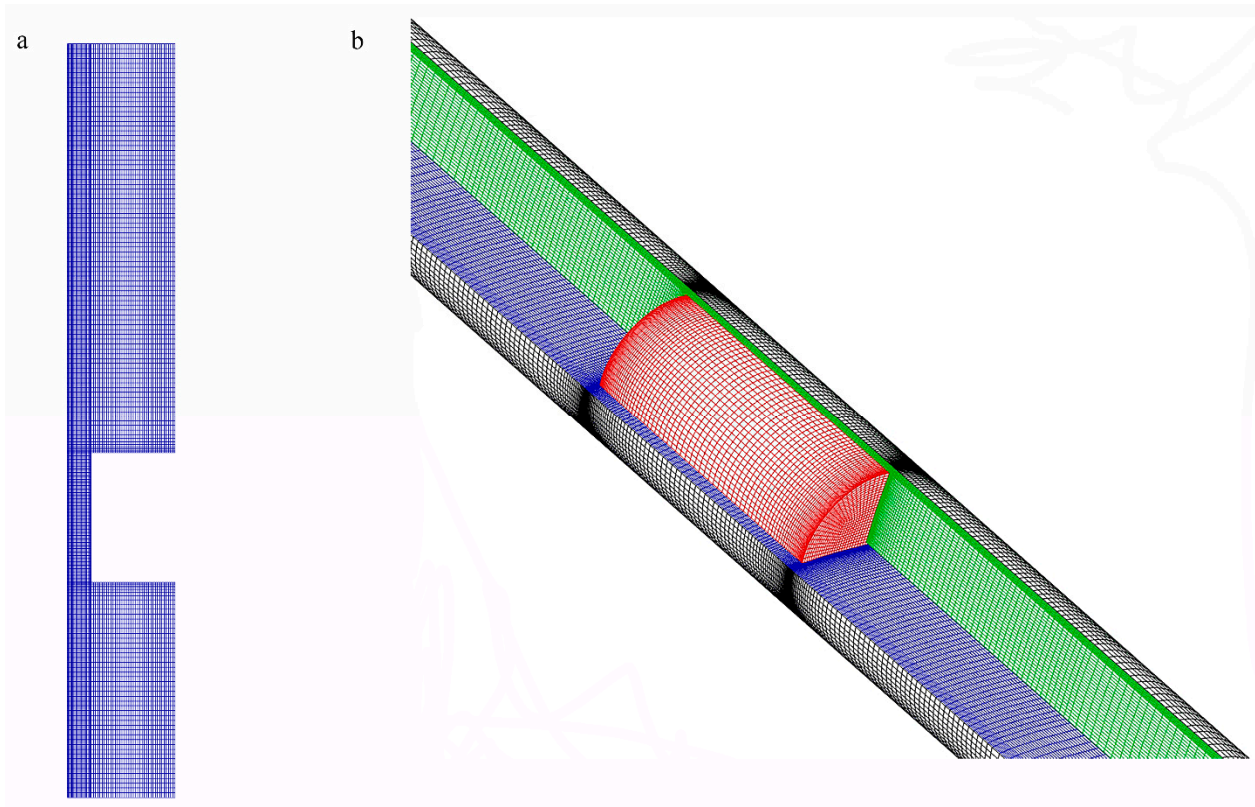
Figure 4. Mesh used for simulation: (**a**) 2D model; (**b**) 3D model.

3.4. Dynamic Mesh Strategy

The ice core transport has been implemented using a dynamic mesh with a layering algorithm because of its superior ability to work with structured mesh under linear movement [22,23]. The technology automatically builds or destroys a row of grids when the ice core's movement exceeds a threshold in a single step. The fluid domain and the ice core are designated to move as the same rigid body in this study, and they both move to the pipe wall as a whole. The mesh is updated in the inlet and outlet zones. The pipe wall is a deformation boundary type, and a new mesh is generated by mapping the original position with the movement of the fluid domain. The fluid domain's inlet and outlet are static areas. Meshes are created at the inlet and deleted at the outlet as the ice cores and fluid domains move. The regional settings are displayed in Table 4.

Table 4. The setting of dynamic mesh zones.

Zone Names	Dynamic Mesh Type
Inlet	Stationary
Outlet	Stationary
Fluid Zone	Rigid Body
Ice Core Wall	Rigid Body
Tube Wall	Deforming

4. Results and Discussion

4.1. Validation of the Numerical Model

The comparison between the experimental and simulated results of the ice core's motion for different lengths with diameters of 62 mm and 66 mm, respectively, is shown in Figure 5. The simulated results of all ice core motions are consistent with the trend of the experimental results, with minor errors. The ice core's displacement and the curve's slope increased with time, indicating that the ice core's movement velocity increased with the increase in displacement. The ice core's displacement and the curve's slope rose over time, suggesting that the ice core's movement velocity also rose. At the same time, the slope of the curve declined as the length of the ice core increased, showing a decrease in the ice core's movement velocity. The ice core's motion duration decreased with the increase in its diameter at the same displacement, suggesting that the ice core's velocity rises as the diameter increases. The movement duration measured in the experiment is 138 ms, the simulation result is 134 ms, and the error is 5% when the ice core displacement is 150 mm, the ice core length is 100 mm, and the diameter is 62 mm. The movement duration measured in the experiment is 60 ms, the simulation result is 56 ms, and the error is 7% when the diameter is 66 mm. The ice core's velocity is still increasing, as seen from the motion curve, and it has not yet achieved the equilibrium condition. The numerical simulation method is effective because the high-speed camera cannot acquire long-distance video due to the field of view and memory limitations.

4.2. The Transport Process of Ice Core

Figure 6 depicts the change in instantaneous velocity and aerodynamic force overtime during ice core transport when the ice-core-to-pipe diameter ratio is 0.88, the ice-core-length-to-diameter ratio is 2, and the eccentricity is 0. Figure 6a demonstrates that, after the ice core begins in a static state, its velocity quickly rises, reaches its maximum after about 1.2 s, and remains almost unchanged. The ice core's maximum velocity increases with an increase in air velocity. As the air velocity increased from 15 m/s to 30 m/s, the ice core's maximum velocity increased from 8.21 m/s to 23.86 m/s.

The ice core is subject to aerodynamic force because its motion is slower than the air's motion, and there is a slip velocity between them. As seen in Figure 6b, the aerodynamic force is most significant at the initial instant because the relative velocity between the ice core and the air is most significant. As the air velocity rises from 15 m/s to 30 m/s, the aerodynamic force rises from 20.82 N to 80.59 N. After starting up, the ice core's velocity increases quickly as the aerodynamic force sharply declines. Regardless of the air velocity, it is eventually reduced to the ice core's buoyant weight and stays that way.

Due to the limitation of the pipe wall, the airflow cross-section around the ice core varies dramatically during transport, and the flow field properties also vary significantly. Figure 7 displays the streamline pattern surrounding the ice core at various times. The ice core is still at the start of the process. All streamlines are forced up against the pipe wall when they enter the annulus region once the flow from the pipe reaches the lower end of the ice core. After the ice core moves, some streamlines follow it forward, while others flow toward the annulus area. The airflow segment abruptly expands at the annulus's exit, and as it moves ahead, a portion of the airflow turns around to backfill the surrounding region above the ice core, creating a vortex zone. The presence of the vortex zone creates a differential pressure force between the upper and lower ends of the ice core. As time

passes, the ice core's velocity rises steadily, the airflow following the movement of the ice core rises, the airflow flowing into the annular region falls, and the vortex area shrinks.
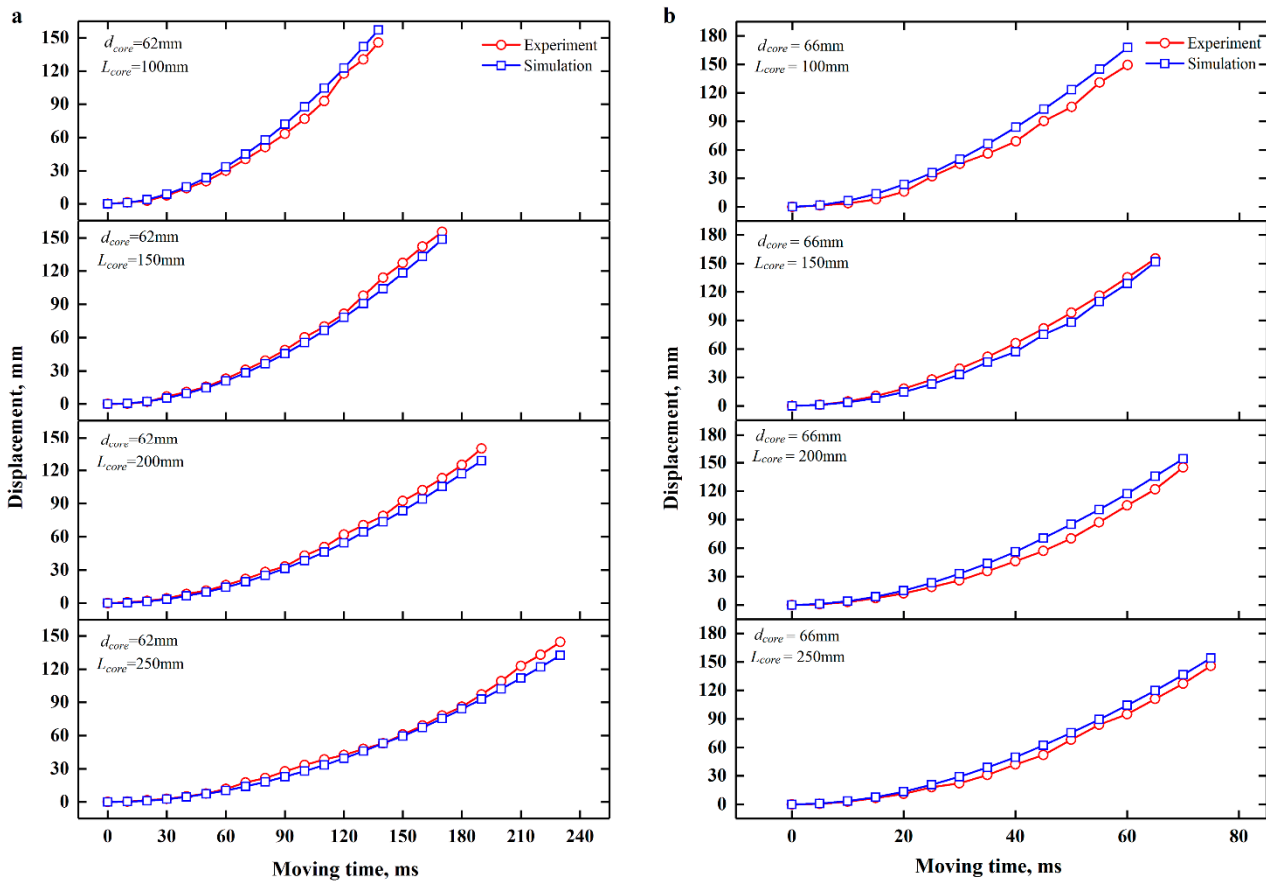
Figure 5. Comparison of experimental and simulated results of ice core motion: (**a**) Ice core diameter of 62 mm; (**b**) Ice core diameter of 66 mm.
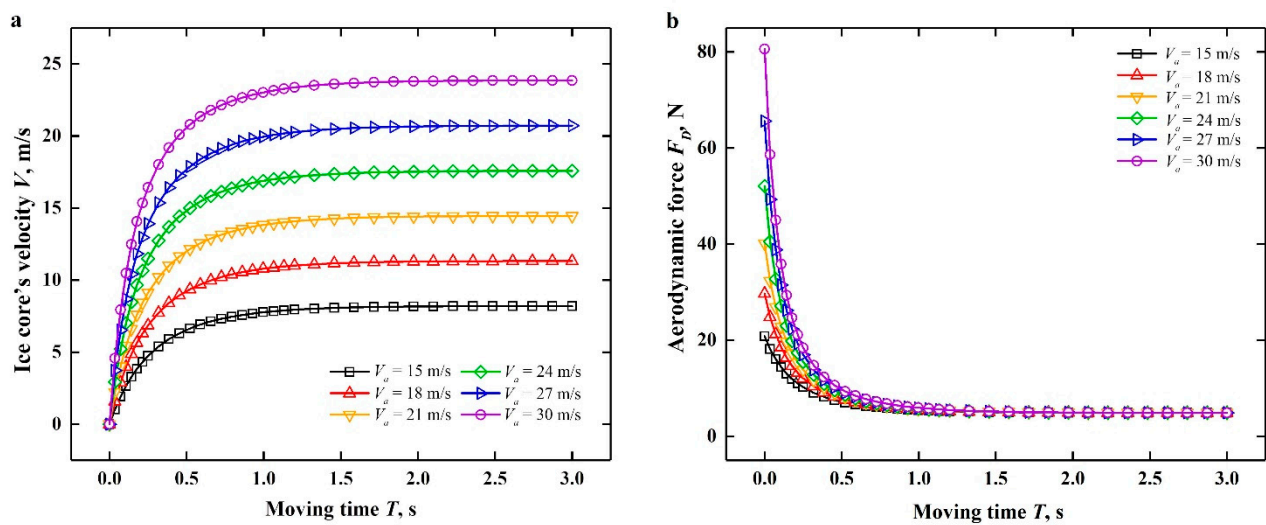
Figure 6. (**a**) Variation of ice core's velocity during transport; (**b**) Variation of the aerodynamic force on the ice core.
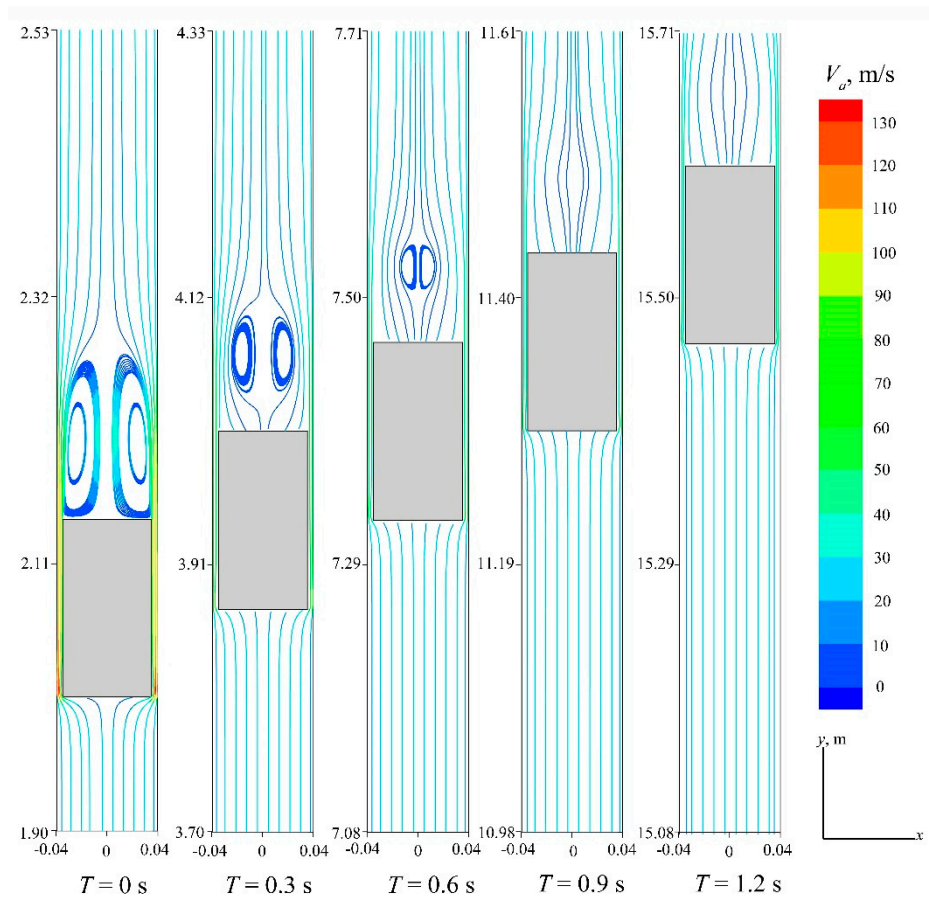
Figure 7. The streamline pattern surrounding the ice core at various times.

It can be seen from the ice core transport process that, at a certain air velocity, the ice core's velocity increases continuously from zero and remains unchanged after reaching the maximum velocity. The maximum velocity of ice core increases with the increase in air velocity. The following discussion will focus on the effects of the ice-core-to-pipe diameter ratio, the ice-core-length-to-diameter ratio, and the eccentricity on the ice core's maximum velocity.

4.3. Effect of the Diameter Ratio on the Ice Core's Maximum Velocity

The effect of the ice-core-to-pipe diameter ratio on the ice core's maximum velocity, V_{max}, at various air velocities is shown in Figure 8a. As air velocity and diameter ratio rise, the value of V_{max} also rises. For a diameter ratio of 0.84, when the air velocity rises from 15 m/s to 30 m/s, the value of V_{max} rises from 5.32 m/s to 21.04 m/s. For the air velocity of 21 m/s, when the diameter ratio increases from 0.80 to 0.92, the value of V_{max} increases from 8.92 m/s to 17.45 m/s. It can be seen from the fitting curve that the maximum velocity, V_{max}, and the air velocity satisfy the linear equation.

The ice core is subjected to aerodynamic force and gravity during its motion, and the aerodynamic force includes pressure difference and friction force. The effect of the diameter ratio on the force of the ice core is depicted in Figure 8b when the air velocity is 21 m/s, and the instantaneous velocity of the ice core is 7 m/s, or when the ice core's slip velocity is 14 m/s. The ice core's buoyant weight is equal, the pressure difference force acting on it rises dramatically with an increase in diameter ratio, and the friction force acting on it is negligible and may be disregarded. As a result, the force generated by the ice core grows with the diameter ratio.

At this time, the streamline pattern near the ice core is shown in Figure 9. When the diameter ratio increases, the gas velocity in the annular space and the vortex zone increase,

resulting in a decrease in the pressure in the vortex zone and an increase in the differential pressure force. Therefore, with the increase in the diameter ratio, the aerodynamic force on the ice core increases.
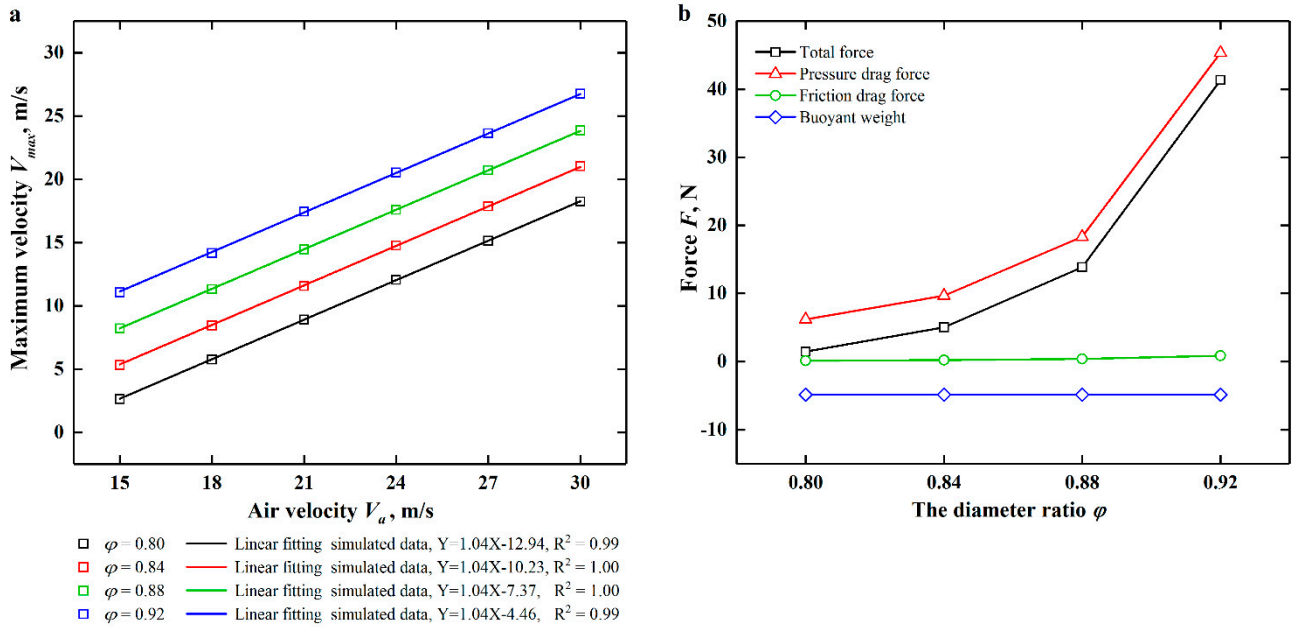
Figure 8. (**a**) Effect of the diameter ratio on the ice core's maximum velocity, V_{max}; (**b**) Effect of the diameter ratio on the force of the ice core.
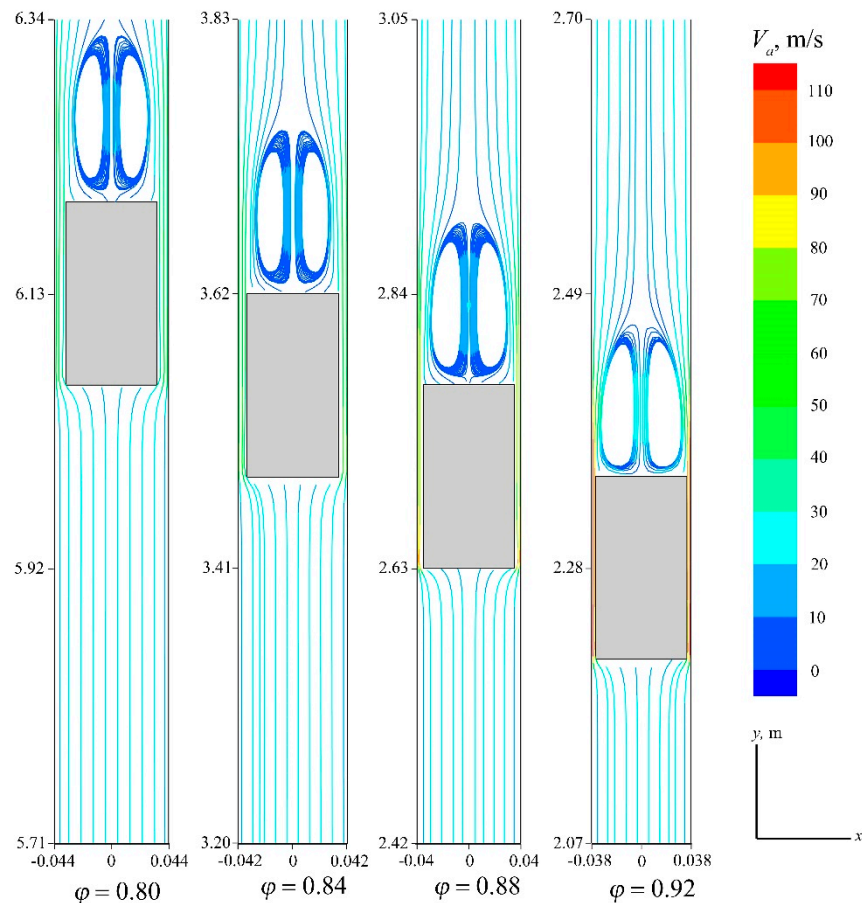
Figure 9. Effect of the diameter ratio on the streamline pattern.

4.4. Effect of the Length-to-Diameter Ratio on the Ice Core's Maximum Velocity

The effect of the length-to-diameter ratio on the ice core's maximum velocity, V_{max}, under various air velocities is shown in Figure 10a. The value of V_{max} increases as air velocity increases and increases as the length-to-diameter ratio decreases. When the air velocity increases from 15 m/s to 30 m/s for the length-to-diameter ratio of 3, the value of V_{max} increases from 7.06 m/s to 22.81 m/s. When the length-to-diameter ratio increases from 1 to 4, the value of V_{max} decreases from 16.22 m/s to 12.50 m/s for the air velocity of 21 m/s. The ice core's maximum velocity, V_{max}, and the air velocity satisfy the linear equation, as seen from the fitting curve.

When the air velocity is 21 m/s and the ice core's velocity is 7 m/s, the length-to-diameter ratio's effect on the ice core's force can be seen in Figure 10b. As the length-to-diameter ratio increases, the buoyant weight of the ice core increases in the negative direction, and the pressure difference force increases in the positive direction. The pressure difference force increase is smaller than the buoyant weight. The frictional force is small and can be neglected. Therefore, the resultant force decreases slightly. As the length-to-diameter ratio increases, the mass of the ice core becomes more significant, and therefore the acceleration becomes smaller.

The streamline pattern near the ice core is shown in Figure 11. Because the diameter ratio of the ice core is equal, the airflow velocity in the annulus between the ice core and the pipe is equal, and the vortex zone size is the same.
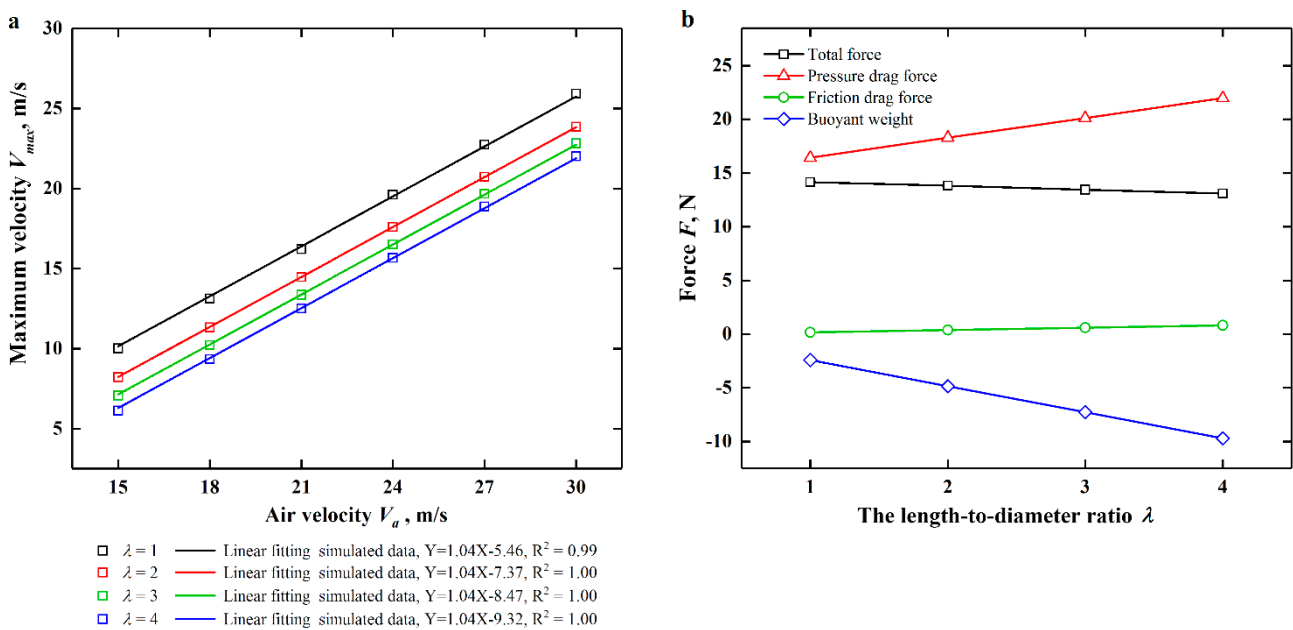
Figure 10. (**a**) Effect of the length-to-diameter ratio on the ice core's maximum velocity, V_{max}; (**b**) Effect of the length-to-diameter ratio on the force of the ice core.

4.5. Effect of the Eccentricity on the Ice Core's Maximum Velocity

The effect of the eccentricity on the ice core's maximum velocity, V_{max}, under different air velocities is shown in Figure 12a. The value of V_{max} increases with the increase in air velocity and eccentricity, but the eccentricity has little effect on the value of V_{max}. For the air velocity of 24 m/s, when the eccentricity increases from 0 to 0.9, the value of V_{max} increases from 17.59 m/s to 17.81 m/s.
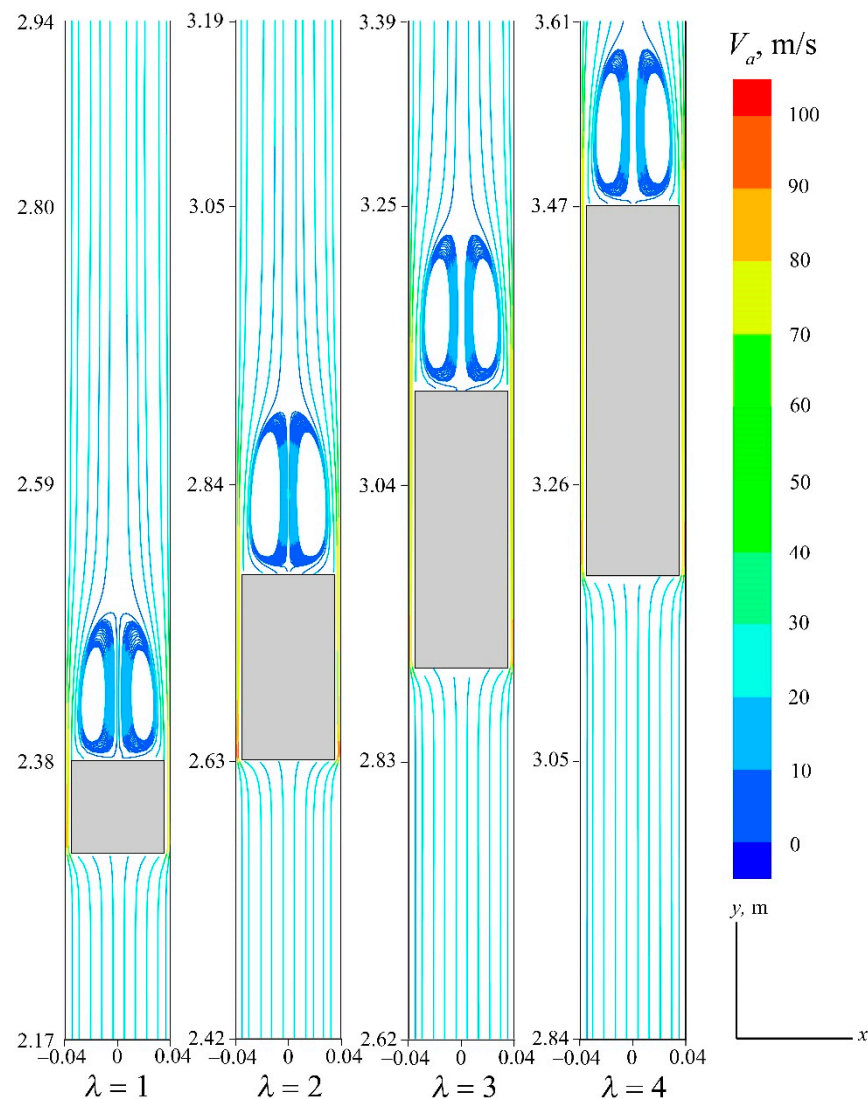
Figure 11. Effect of the length-to-diameter ratio on the streamline pattern.

When the air velocity is 21 m/s, and the instantaneous velocity of the ice core is 7 m/s, the eccentricity's effect on the ice core's force is shown in Figure 12b. With the increase in eccentricity, the buoyant weight and friction force are unchanged, and the pressure difference force gradually increases, but the increase is slight, so the resultant force only increases slightly.

The streamline pattern around the ice core is shown in Figure 13. With the increased eccentricity, the airflow on the broad side of the annular space increases, and the vortex area formed by the airflow on both sides change from symmetric distribution to asymmetric distribution. When the eccentricity is 0.6, the vortex region formed on the broad side of the annular space is further expanded, and the vortex region formed on the narrow side is reduced. When the eccentricity is 0.9, the vortex region formed on the broad side reaches the maximum, and the vortex region on the narrow side disappears. It can be seen from the streamline diagram of air flow under different eccentricity that with the increase in eccentricity, the vortex area above the ice core increases, which increases the aerodynamic force on the ice core. However, the dynamic viscosity of air is very small, so the aerodynamic force increases less.
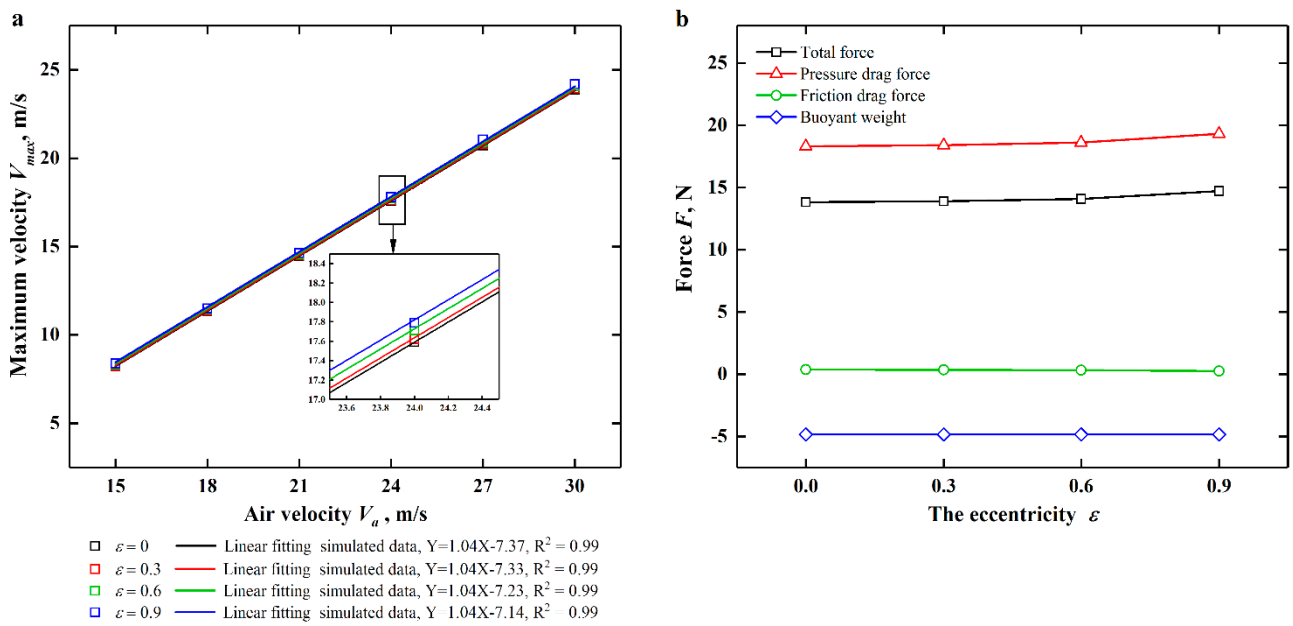
Figure 12. (**a**) Effect of the eccentricity on the ice core's maximum velocity, V_{max}; (**b**) Effect of the eccentricity on the force of the ice core.
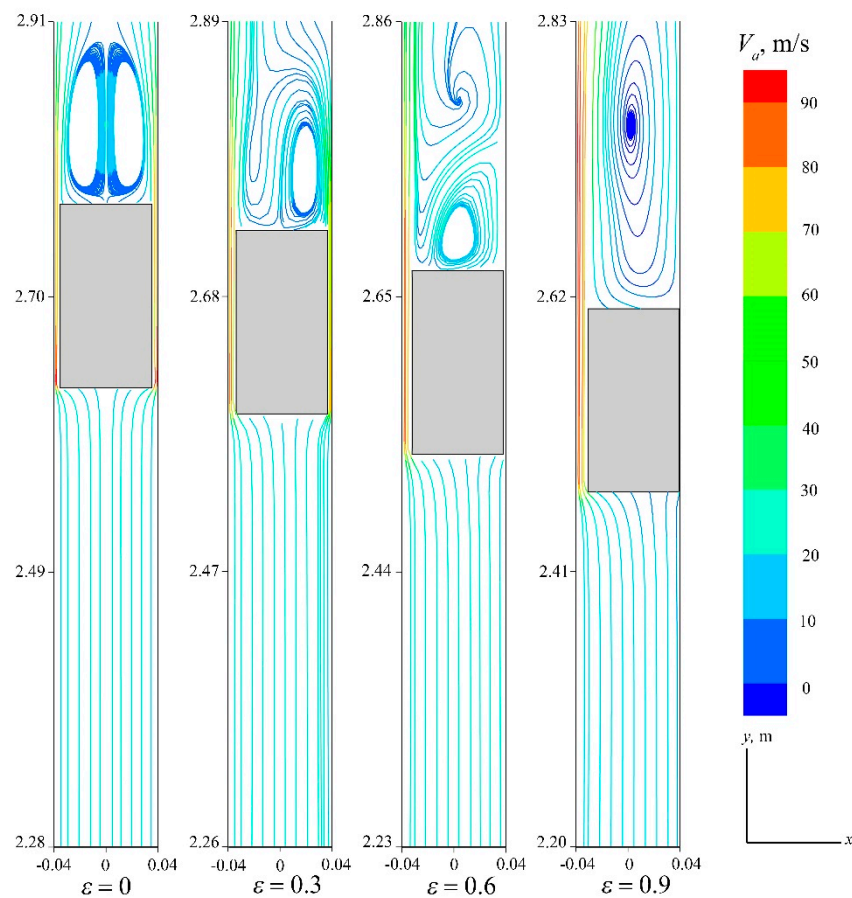
Figure 13. Effect of the eccentricity on the streamline pattern.

4.6. Prediction of the Ice Core's Maximum Velocity

According to the fitting curve of the ice core's maximum velocity, V_{max}, under different diameter ratios, length-to-diameter ratios, and eccentricities, the ice core's maximum velocity V_{max}, satisfies the linear equation:

$$V_{max} = a + bV_a \tag{7}$$

Among them, the a-value is more related to the diameter and length-to-diameter ratios and is mainly independent of the eccentricity. The b-value is always 1.04, independent of the geometric characteristics of the ice core and pipe. According to the similarity principle, it can be considered that when $0.80 \leq \varphi \leq 0.92$, $1 \leq \lambda \leq 4$, $0 \leq \varepsilon \leq 0.9$ in pneumatic conveying, the maximum velocity of the cylindrical object satisfies Equation (7). The structural form of this equation is similar to the equation of capsule velocity in hydraulic transportation. Notice that V_{max} is precisely 0 when the air velocity, V_0, is the suspension velocity of the ice core at this time. Substituting into Equation (7) yields:

$$a = -1.04V_0 \tag{8}$$

$$V_{max} = -1.04V_0 + 1.04V_a \tag{9}$$

where V_a is the airflow velocity.

The ice core's maximum velocity, V_{max}, can be determined by the suspension velocity, V_0, of the ice core. In the following, the suspension velocity of the ice core is solved by CFD simulation. When the ice core is suspended, the velocity of the ice core is zero, and the aerodynamic force is equal to the buoyant weight.

The aerodynamic force on the ice core is:

$$F_D = \frac{1}{2}C_D\rho_a A_s u_r^2 \tag{10}$$

The buoyant weight of the ice core is:

$$F_W = A_s L(\rho_i - \rho_a)g \tag{11}$$

where C_D is the drag coefficient of the ice core, which is related to the particle Reynolds number, Re_p, of the ice core [24], ρ_a and ρ_i are the air and ice core densities, respectively, A_s is the cross-sectional area of the ice core, L is the length of the ice core, u_r is the velocity difference between the airflow and the ice core, and u_r is equal to the suspension velocity, V_0, when the ice core is suspended.

The cross-sectional area of the ice core is:

$$A_s = \frac{1}{4}\pi d^2 \tag{12}$$

The Reynolds number of the ice core is:

$$Re_p = \frac{\rho_a u_r d}{\mu} \tag{13}$$

where d is the ice core diameter and μ is the dynamic viscosity of air.

Simultaneous Equations (10)–(12) are used to obtain the suspension velocity:

$$u_r = V_0 = \sqrt{\frac{2L(\rho_i - \rho_a)g}{C_D\rho_a}} \tag{14}$$

The CFD simulation can be used to find the aerodynamic force of the ice core at a static state with different particle Reynolds numbers; the drag coefficient can be obtained from Equation (10), and the suspension velocity can be obtained from Equation (14). The

simulation results of the drag coefficient of the ice core are shown in Figure 14. The results show that the drag coefficient of the ice core in double logarithmic coordinates satisfies a linear relationship with the Reynolds number. The drag coefficient decreases with increasing Reynolds number and increases with increasing diameter ratio and length-to-diameter ratio, which is consistent with the trend obtained from related studies [24].
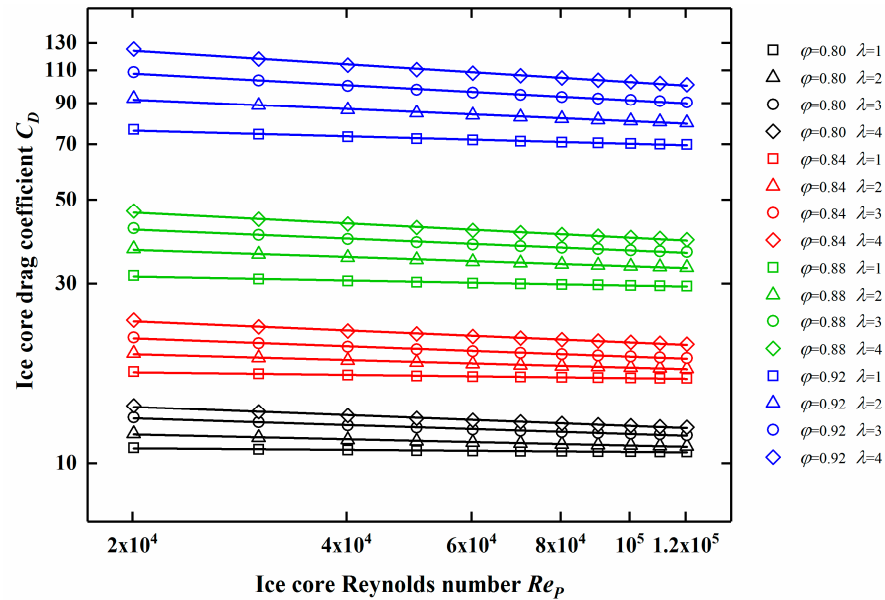
Figure 14. Simulated data of the drag coefficient of the ice core.

According to the simulation results, the drag coefficient of the ice core satisfies the equation:

$$\text{Log}C_D = A + B\text{Log}Re_p \tag{15}$$

Simultaneous Equations (13)–(15) can be obtained:

$$V_0 = \left(2 \times 10^{-A} g(\rho_i - \rho_a)\rho_a^{-B-1}\lambda\mu^B d^{(1-B)}\right)^{\frac{1}{2+B}} \tag{16}$$

where A and B are equations concerning φ, λ. Assuming:

$$A = f(\varphi, \lambda) \tag{17}$$

$$B = f(\varphi, \lambda) \tag{18}$$

By fitting the simulation data with the Levenberg–Marquardt method and the general global optimization method in the professional data fitting software 1st Opt, the following results are obtained:

$$A = (0.0292 + 0.2389\varphi + 0.0853\lambda - 0.0132\lambda^2 + 0.0009\lambda^3)/(1 - 0.9327\varphi + 0.0131\lambda - 0.0017\lambda^2) \tag{19}$$

$$B = 0.02917 + 0.2389\varphi^{0.0853} - 0.0132\lambda^{0.0009} - 0.9327\varphi^{0.0853}\lambda^{0.0009} \tag{20}$$

The correlation coefficient of the fitting equation reached 0.99. The suspension velocity of the ice core can be obtained by simultaneous Equations (16), (19) and (20). To verify the accuracy of this suspension velocity model, the predicted values of the model are compared with the experimental values, as shown in Table 5. The maximum error of the predicted values of the model is less than 10%, and the average error of all predicted values is 6.6%, which indicates that the suspension velocity model proposed in this paper has high accuracy and can be used to predict the suspension velocity of a cylindrical object in

a vertical pipe. The ice core's maximum velocity, V_{max}, can be found by substituting the suspension velocity into Equation (9).

Table 5. Comparison of predicted and experimental values of the suspension velocity model.

Pipe Dimmeter mm	Ice Core Dimmeter mm	Ice Core Length mm	Experimental Data m/s	Calculated Data m/s	Error %	Average Error %
67	60	100	5.23	5.73	9.56	
67	60	150	7.14	6.83	−4.34	
67	60	200	8.04	7.24	−9.95	
71	60	100	8.21	8.87	8.04	
71	60	150	10.64	10.64	0.00	6.63
71	60	200	12.26	11.64	−5.06	
89	80	100	5.01	5.47	9.18	
89	80	150	6.59	6.37	−3.34	
89	80	200	7.83	7.19	−8.17	
89	80	250	8.17	7.46	−8.69	

5. Conclusions

In this paper, CFD dynamic mesh technology, which experiments have fully verified, is used to simulate the transport process of the ice core at different air velocities, and the effect of the ice-core-to-pipe diameter ratio, ice-core-length-to-diameter ratio, and eccentricity on the ice core's maximum velocity are investigated. The equation of the maximum velocity is obtained by curve fitting. This paper's results can act as a guide to solving the movement velocity of a cylindrical object in a pneumatic conveying pipe. The main conclusions are as follows:

1. In the transport process, the ice core's velocity increases rapidly and remains unchanged after reaching the maximum velocity. The ice core's maximum velocity increases with the increase in air velocity. For the ice core with a diameter ratio of 0.88 and the length-to-diameter ratio of 2, when the air velocity increases from 15 m/s to 30 m/s, the ice core's maximum velocity increases from 8.21 m/s to 23.86 m/s.

2. The ice core's maximum velocity increases with the diameter ratio and decreases with the length-to-diameter ratio. The effect of eccentricity on the maximum velocity is slight. When the air velocity reaches 21 m/s, the diameter ratio for the ice core with a length-to-diameter ratio of 2 increases from 0.80 to 0.92, and the maximum velocity increases from 8.92 m/s to 17.45 m/s.

3. During the ice core transport, the airflow forms a vortex zone above the ice core, and the vortex zone's size decreases with the ice core' velocity increase. When the eccentricity of the ice core is 0, the vortex area is symmetrically distributed, and when it is eccentric, it is asymmetrically distributed, and the more significant the eccentricity, the stronger the asymmetry.

4. The ice core's maximum velocity, V_{max}, and the air velocity satisfy the equation $V_{max} = -1.04V_0 + 1.04V_a$. V_0 is the suspension velocity of the ice core, and V_0 can be obtained from the suspension velocity model of the ice core by the CFD simulation method.

Author Contributions: Conceptualization: P.C. and M.W.; methodology: W.H. and M.W.; formal analysis: P.C. and M.W.; writing—original draft: M.W.; writing—review and editing: B.Q. and J.C. (Jine Cao); validation: M.W. and J.C. (Jingchao Chen); investigation: M.W. and W.H.; project administration: P.C. All authors have read and agreed to the published version of the manuscript.

Institutional Review Board Statement: Not applicable.

Informed Consent Statement: Not applicable.

References

1. Hoffmann, H.M.; Grieman, M.M.; King, A.C.F.; Epifanio, J.A.; Martin, K.; Vladimirova, D.; Pryer, H.V.; Doyle, E.; Schmidt, A.; Humby, J.D.; et al. The ST22 chronology for the Skytrain Ice Rise ice core—Part 1: A stratigraphic chronology of the last 2000 years. *Clim. Past* **2022**, *18*, 1831–1847. [CrossRef]
2. Újvári, G.; Klötzli, U.; Stevens, T.; Svensson, A.; Ludwig, P.; Vennemann, T.; Gier, S.; Horschinegg, M.; Palcsu, L.; Hippler, D.; et al. Greenland ice core record of recent glacial dust sources and atmospheric circulation. *J. Geophys. Res. Atmos.* **2022**, *127*, e2022JD036597. [CrossRef] [PubMed]
3. Talalay, P. *Mechanical Ice Drilling Technology*; Springer: Singapore, 2016.
4. Talalay, P. *Thermal Ice Drilling Technology*; Springer: Singapore, 2020.
5. Talalay, P.; Li, X.; Gong, D.; Fan, X.; Zhang, N.; Yang, Y. Design and experiment of clamper used in Antarctic subglacial bedrock drilling. *J. Mar. Sci. Eng.* **2019**, *7*, 153. [CrossRef]
6. Talalay, P. Perspectives for development of ice-core drilling technology: A discussion. *Ann. Glaciol.* **2014**, *55*, 339–350. [CrossRef]
7. Wang, M.; He, W.; Wang, M.; Cao, J.; Cao, P. Numerical Simulation Study of a Swirling Drill Bit Used for Ice Core Drilling. *J. Mar. Sci. Eng.* **2022**, *10*, 296. [CrossRef]
8. Talalay, P.; Yang, C.; Cao, P.; Wang, R.; Zhang, N.; Fan, X.; Yang, Y.; Sun, Y. Ice-core drilling problems and solutions. *Cold Reg. Sci. Technol.* **2015**, *120*, 1–20. [CrossRef]
9. Wang, R.; An, L.; Cao, P.; Chen, B.; Sysoev, M.; Fan, D.; Talalay, P. Rapid ice drilling with continual air transport of cuttings and cores: General concept. *Polar Sci.* **2017**, *14*, 21–29. [CrossRef]
10. Hu, Z.; Talalay, P.; Zheng, Z.; Cao, P.; Shi, G.; Li, Y.; Fan, X.; Ma, H. Air reverse circulation at the hole bottom in ice-core drilling. *J. Glaciol.* **2019**, *65*, 149–156. [CrossRef]
11. Gibson, C.; Boeckmann, G.; Meulemans, Z.; Kuhl, T.; Koehler, J.; Johnson, J.; Slawny, K. RAM-2 Drill system development: An upgrade of the Rapid Air Movement Drill. *Ann. Glaciol.* **2021**, *62*, 99–108. [CrossRef]
12. Bolshunov, A.V.; Vasilev, D.A.; Ignatiev, S.A.; Dmitriev, A.N.; Vasilev, N.I. Mechanical drilling of glaciers with bottom-hole scavenging with compressed air. *Led I Sneg. Ice Snow* **2022**, *62*, 35–46. [CrossRef]
13. Cao, P.; Liu, M.; Chen, Z.; Chen, B.; Zhao, Q. Theory calculation and testing of air injection parameters in ice core drilling with air reverse circulation. *Polar Sci.* **2018**, *17*, 23–32. [CrossRef]
14. Cao, P.; Cao, H.; Cao, J.; Liu, M.; Chen, B. Studies on pneumatic transport of ice cores in reverse circulation air drilling. *Powder Technol.* **2019**, *356*, 50–59. [CrossRef]
15. Jägers, J.; Wirtz, S.; Scherer, V.; Behr, M. Experimental analysis of wood pellet degradation during pneumatic conveying processes. *Powder Technol.* **2020**, *359*, 282–291. [CrossRef]
16. Unnikrishnan, A.; Chhabra, R.P. An experimental study of motion of cylinders in newtonian fluids: Wall effects and drag coefficient. *Can. J. Chem. Eng.* **1991**, *69*, 729–735. [CrossRef]
17. Lau, R.; Hassan, M.S.; Wong, W.; Chen, T. Revisit of the wall effect on the settling of cylindrical particles in the inertial regime. *Ind. Eng. Chem. Res.* **2010**, *49*, 8870–8876. [CrossRef]
18. Latto, B.; Chow, K.W. Hydrodynamic transport of cylindrical capsules in a vertical pipeline. *Can. J. Chem. Eng.* **1982**, *60*, 713–722. [CrossRef]
19. MysKa, J.; Vlasak, P. The dependence of coefficients in the relation of velocity ratio on parameters of a capsule. *Chem. Eng. Sci.* **1983**, *38*, 547–555. [CrossRef]
20. Yao, B.; Ding, Q.; Zhang, K.; Yang, D.; Zhu, X. Translation simulation of a cylinder in a horizontal pipe. *Eng. Appl. Comp. Fluid Mech.* **2019**, *13*, 1106–1118. [CrossRef]
21. Yang, D.; Xing, B.S.; Li, J.; Wang, Y.; Hu, N.; Jiang, S. Experiment and simulation analysis of the suspension behavior of large (5–30 mm) nonspherical particles in vertical pneumatic conveying. *Powder Technol.* **2019**, *354*, 442–455. [CrossRef]
22. Liu, M.; Zhu, C.; Cui, T.; Zhang, H.; Zheng, W.; You, S. An alternative algorithm of tunnel piston effect by replacing three-dimensional model with two-dimensional model. *Build. Environ.* **2018**, *128*, 55–67. [CrossRef]
23. Xue, P.; You, S.; Chao, J.; Ye, T. Numerical investigation of unsteady airflow in subway influenced by piston effect based on dynamic mesh. *Tunn. Undergr. Space Technol.* **2014**, *40*, 174–181. [CrossRef]
24. Ren, B.; Zhong, W.; Jin, B. Study on the Drag of a Cylinder-Shaped Particle in Steady Upward Gas Flow. *Ind. Eng. Chem. Res.* **2011**, *50*, 7593–7600. [CrossRef]